Excitonic Properties of Low Bandgap Lead-Tin Halide Perovskites

Krzysztof Galkowski,†,‡,¶ Alessandro Surrente,† Michal Baranowski,†,§ Baodan Zhao,‡ Zhuo Yang†, Aditya Sadhanala,‡ Sebastian Mackowski,¶ Samuel D. Stranks,‡ and Paulina Plochocka†

†Laboratoire National des Champs Magnetiques Intenses, CNRS-UGA-UPS-INSA, Grenoble and Toulouse, 143 Avenue de Rangueil, 31400 Toulouse, France

‡Cavendish Laboratory, University of Cambridge, JJ Thomson Avenue, Cambridge CB3 0HE, UK

¶Institute of Physics, Faculty of Physics, Astronomy and Informatics, Nicolaus Copernicus University, 5th Grudziadzka St., 87-100 Torun, Poland

§Department of Experimental Physics, Faculty of Fundamental Problems of Technology, Wroclaw University of Science and Technology, 27 Wyb. Wyspiańskiego St. 50-370 Wroclaw, Poland

E-mail: sds65@cam.ac.uk, paulina.plochocka@lncmi.cnrs.fr

Abstract

The $MAPb_{1-x}Sn_xI_3$ (x=0 - 1) (MA=methylammonium) perovskite family comprises a range of ideal absorber bandgaps for single- and multijunction perovskite solar cells. Here, we use spectroscopic measurements to reveal a range of hitherto unknown fundamental properties of this materials family. Temperature-dependent transmission results show that the temperature of the tetragonal to orthorhombic structural transition decreases with increasing tin content. Through low temperature magneto-spectroscopy, we show that the exciton binding energy is lower than 16 meV, revealing that the dominant photo-generated species at typical operational conditions of optoelectronic devices are free charges rather than excitons. The reduced mass increases approximately proportionally to the bandgap, and the mass values (0.075 - 0.090m_e) can be described with a two-band k□p perturbation model extended across

the broad bandgap range 1.2 - 2.4 eV. Our findings can be generalized to predict values for the effective mass and binding energy for other members of this family of materials.

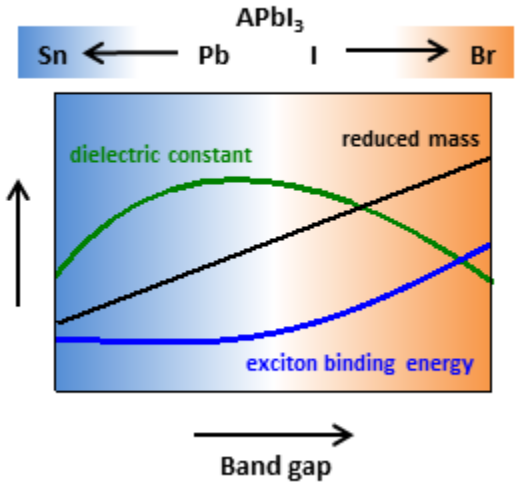

Hybrid organic inorganic perovskites have shown tremendous performance in photovoltaic devices and, recently, in a variety of other optoelectronic applications including light emitting diodes[1,2], lasers[3,4] and photodetectors[5,6]. They possess remarkable properties including strong light absorption[7], tunable bandgaps[8,9], long carrier diffusion lengths[10,11], which are combined with easy and low-cost fabrication[12,13], lending them to a large variety of device applications. HOIPs take the perovskite ABX_3 crystal structure, where the A-site is typically occupied by a small organic cation such as Methylammonium (MA) or Formamidinium (FA), B is a divalent metal cation such as lead (Pb) or tin (Sn), and X is a halide anion (Cl, Br, I). The majority of work to date has utilized Pb-based perovskites in which the bandgap exceeds 1.5 eV. To reach the optimum power conversion efficiency (PCE) in a single junction, the bandgap of the active material has to be pushed down to 1.3 eV[14]. Hence, developing perovskites with lower bandgaps is highly desirable for photovoltaic applications as well as for near-infrared light emitters and photo-detectors. Importantly, perovskite-perovskite tandem solar cells, one of the most promising applications for perovskites, require a bottom cell with low bandgap (0.9-1.2 eV) to optimally generate power when coupled with wide bandgap (1.7-1.9 eV) perovskites[15,16].

Recently, Sn-based hybrid perovskites have been exploited to lower the bandgaps below 1.5 eV. The first optical measurements performed on $MASnI_3$ perovskites showed bandgaps of ~1.3 eV combined with promising performance in PV devices, reaching power conversion efficiencies of 6%[17,18]. However, these pure tin perovskites are generally highly unstable due to a rapid self-doping through oxidation of Sn^{2+} to Sn^{4+}; even despite PCEs more recently reaching 9%[19], performances remain well below their Pb-based counterparts (23%)[20,21]. An alternative strategy to lower the bandgap is through partial substitution of the Pb by Sn, for example $MAPb_{1-x}Sn_xI_3$ (where x=0 – 1) [22–25]. In this case, the bandgap does not monotonically decrease with increasing fraction of Sn (x) with a minimum at x=0.5-0.8[22–25]. The origin of this bowing is still debated, with relativistic[23,26] and steric effects[23,27], or an energy mismatch between Pb and Sn orbitals[28] being proposed as possible explanations; we note that such a bowing phenomenon is also seen in many other alloyed semiconductors[29,30]. The mixed lead-tin compositions are typically much more stable against self-oxidation processes than the pure tin counterparts, with optimal thermal and operational stability appearing for x<0.5[31,32]. As a result of optimization of the fabrication methods and the compositions, the PCEs of Pb:Sn alloy perovskite-based solar cells have recently reached 17.8% for single junction[33] and over 19% for tandem perovskite-perovskite configurations utilizing a Pb:Sn absorber layer as the bottom cell[32]. There are also promising reports of light emission from Pb-Sn-based perovskite emitters[34,35]. Although device performances are still far from their predicted limits (for example >30% PCE for tandem solar cells[16]), these reports demonstrate that the alloyed lead-tin materials are promising candidates for optoelectronic applications.

Nevertheless, despite recent progress in device performance, the lead-tin perovskite alloys are still at an early stage of development. Important parameters critical for the design of a PV cell such as the exciton binding energy and dielectric constant, as well as the temperature evolution of the crystal structure and the presence of phase transitions, have not been yet experimentally studied in this material family. Determination of these fundamental electronic properties is crucial

for understanding the operation and efficiency limiting factors in these low bandgap materials, which will in turn drive further performance improvements.

In this work, we present a comprehensive study of optical and electronic properties of mixed lead-tin $MAPb_{1-x}Sn_xI_3$ hybrid perovskite thin films. Temperature-dependent absorption measurements provide clear evidence for a structural phase transition from tetragonal to orthorhombic in the temperature range ~100-150 K, akin to those seen in other families of hybrid organic-inorganic compounds. The phase transition temperature shifts towards lower values with an increasing tin to lead ratio. Using high-field magneto-spectroscopy, we directly determine the exciton binding energy (R^*) and reduced mass (μ) of the mixed lead-tin perovskite systems. We show that μ follows the band gap according to an empirical two-band model across the broad bandgap range 1.2 - 2.4 eV, a much wider range than derived previously[36–38]. We also find that the exciton binding energy is low compared to the thermal energy at room temperature, revealing that under solar illumination the dominant photo-generated species are free electrons and holes which can be easily collected at device electrodes without further complicated heterojunctions. Further, our data indicate that the substitution of Pb with lighter Sn ions increases the energy of octahedral phonon modes, reducing the effective dielectric constant. Our results reveal key physical parameters that are critical to an absolute understanding of the low bandgap mixed lead-tin perovskite semiconductors and their device implementation.

We solution processed $MAPb_{1-x}Sn_xI_3$ (x=0.0, 0.2, 0.4, 0.6, 0.8, 1) thin films on fused silica substrates using a hot casting recipe[24] (see Methods for further details). Briefly, appropriate fractions of $MAPbI_3$ and $MASnI_3$ precursor components in *N,N*-dimethylformamide (DMF) were combined to make precursor solutions with the desired fraction of Sn (x), and the solutions heated to 80 °C. The substrates were heated to 240 °C and loaded quickly onto the spin coater chuck, and the hot solutions deposited onto the substrate and subsequently spin coated at 4000 rpm

for 10 seconds, then the coated substrate immediately shifted to a hot plate for annealing at 100 °C for 10 min.

Typical temperature dependent transmission spectra for the x=0, 0.4 and 0.8 compositions are shown in Fig. 1 a, b and c, respectively, (see Fig. S1, Supporting Information, for the x=0.2, 0.6 and 1.0 compositions). Starting the experiment at low temperature (T = 4.2 K), we find that the spectra consist of a single absorption minimum. We attribute this minimum to the 1s excitonic absorption of the orthorhombic crystalline phase, the phase in which the octahedra of Pb and Sn halide perovskites equilibrate at low temperatures[39,40]. As we increase the temperature, we observe a blue shift of the 1s transition. In the range of 100-150 K, another absorption minimum appears at lower energy, which is followed by a vanishing of the high-energy transition. Heating further up to room temperature, the absorption energy of the remaining low-energy minimum continues to increase.

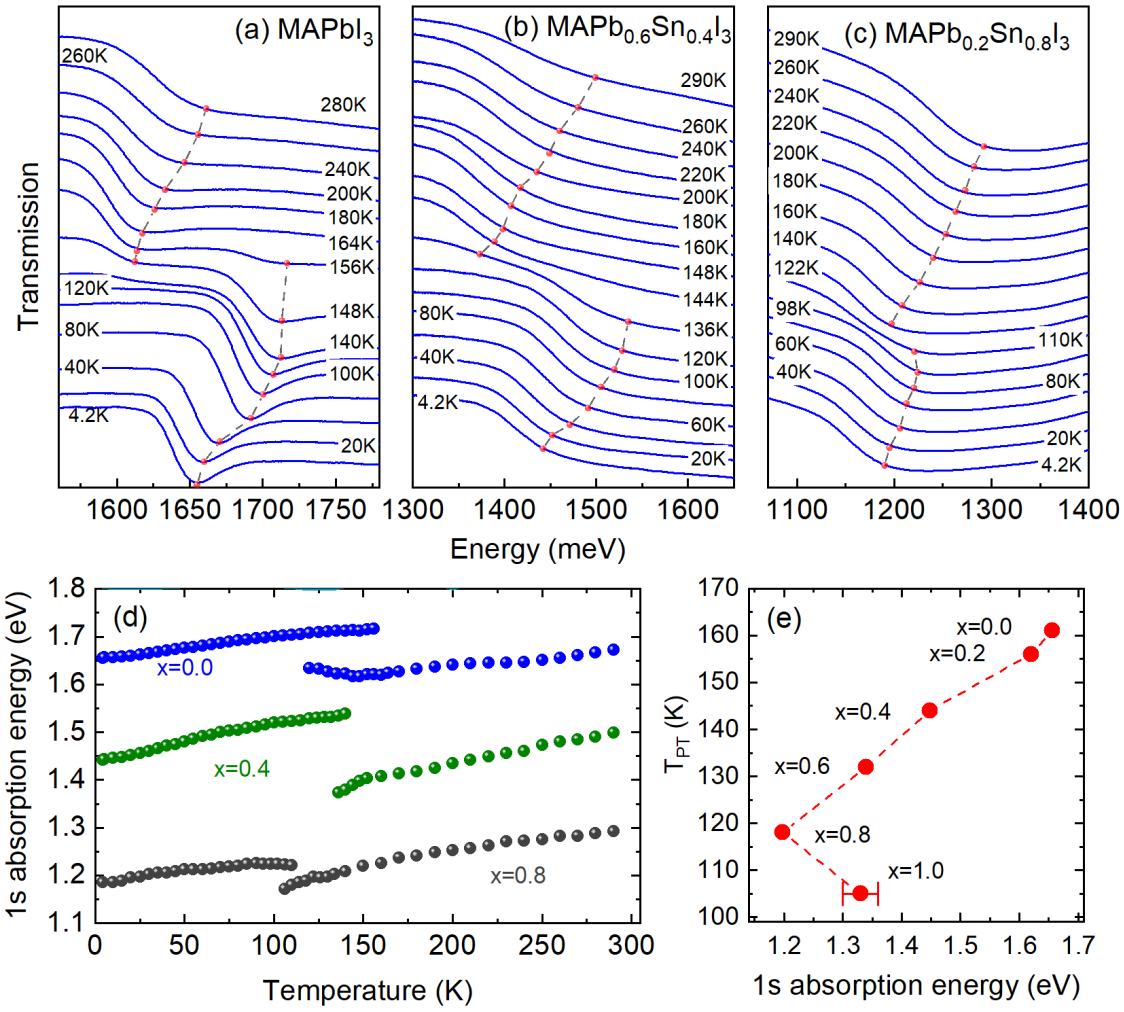

Figure 1. Transmission spectra measured at different temperatures for (a) $MAPbI_3$, (b) $MAPb_{0.6}Sn_{0.4}I_3$ and (c) $MAPb_{0.2}Sn_{0.8}I_3$ thin films, respectively. The points and dashed lines are a guide for the eye to follow the absorption minima. (d) Absorption energy as a function of temperature for $MAPb_{1-x}Sn_xI_3$ compounds. (e) Phase transition temperature (T_{PT}) as a function of 1s absorption energy.

To further understand the temperature-dependent behavior, we plot the absorption energy for each composition as a function of temperature in Fig. 1(d) (see Fig. S2, Supporting Information, for other compositions). Across the entire temperature range, we observe that the absorption energy (ascertained from the transmission minima) decreases with increasing fraction of Sn across the range $0.0 \leq x \leq 0.8$, before rising again for the x=1.0 composition. This is in agreement with earlier works on Pb:Sn perovskites which reported bowing in the bandgap behavior, with the minimum falling between x = 0.5-0.8[22–25], and x = 0.8

being the reported value for the films prepared with the hot-cast method used in this study[24]. In all studied compositions we also find an increase in the bandgap as we increase the temperature. Such phenomenon is typical for lead halide perovskites and we now report similar behavior for Pb-Sn analogues. Briefly, in metal halide perovskites the bandgap is significantly reduced by strong spin orbit coupling (SOC) resulting from the presence of the heavy B-site cation (Pb and/or Sn)[41,42]; as the interatomic distance increases with temperature, the weakening of the SOC splitting broadens the bandgap[43,44].

We also observe an abrupt bandgap drop in the intermediate temperature range (~100 - 150 K) for all Pb:Sn ratios. We attribute this change to the structural transition from the low-temperature orthorhombic phase to more symmetric structures at higher temperature, which has been observed for the lead halide perovskite[37,39,45] and also in $MASnI_3$[40,46]. As shown in Fig. 1(e), the phase transition temperature (T_{PT}) gradually decreases as we increase the Sn content (x) from around 160 K for $MAPbI_3$ (x=0.0) to 105 K for $MASnI_3$ (x=1.0). We explain this by considering that the average size of the BX_6 octahedra reduces as smaller Sn replace Pb ions, allowing the straightening of B-X-B bonds at shorter lattice constants and, thus, lowering the temperature for structural transitions. This reasoning is in agreement with earlier studies of octahedral tilting in $MAPb_{1-x}Sn_xI_3$ compounds at room temperature, i.e., higher Sn content was found to reduce the lattice distortion, which leads to a transformation from tetragonal at low Sn contents (x≈0) to quasi-cubic trigonal structure at room temperature for $x \approx 0.5$[23]. Finally, we find that the bandgap drop when moving through the phase transition (from low to high temperature), in which the structural symmetry increases[47], is largest for x = 0.4. It is possible that lattice contraction effects become most pronounced for an equal distribution of smaller (Sn) and larger (Pb) octahedra, which was previously suggested to have an impact on the bandgap value[23,27].

We now perform magneto-transmission spectroscopy of thin films in the $MAPb_{1-x}Sn_xI_3$ series to directly determine the binding energy and reduced mass of the exciton. In Fig. 2(a), we present typical transmission spectra for $MAPb_{0.2}Sn_{0.8}I_3$, measured at different values of magnetic field at 2 K (see Fig. S3 and S4 for x=0.6,

respectively, and Fig. S5 for absolute transmission scale). At zero magnetic field, the spectrum is dominated by one pronounced minimum, centered at 1180 meV, which we attribute to the 1s excitonic state. The energy of this minimum blue shifts with increasing magnetic field.

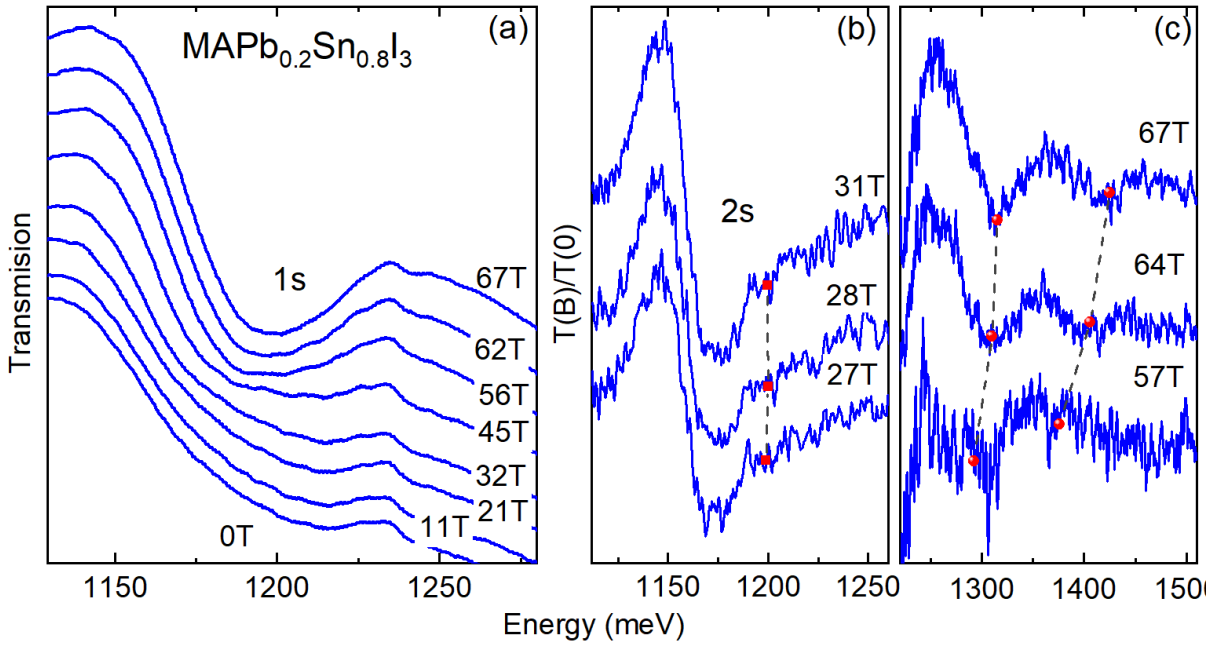

Figure 2: Low temperature (2 K) magneto-transmission spectra for a $MAPb_{0.2}Sn_{0.8}I_3$ thin film. (a) Transmission spectra measured at the indicated magnetic field values. Transmission spectra in magnetic field divided by a zero field spectrum showing (b) the minima of 2s excitonic and (c) free-carrier transitions. The points and dashed lines are a guide for the eye.

To reveal higher energy transitions, we plot differential transmission spectra obtained by dividing the transmission spectrum at $B \neq 0$ T by the spectrum measured at zero magnetic field (in Fig. 2(b)). Such spectral ratios are dominated by a large differential feature, originating from the blue-shifted 1s state. On its high energy side, a very weak 2s minimum appears at magnetic fields $B \approx 30$ T. In the higher energy range (Fig. 2(c)), equally spaced absorption minima appear consecutively as the magnetic field is further increased; these minima correspond to free carrier transitions between Landau levels in the valence and conduction bands .

Next, we extract the energies ascertained from the absorption minima and plot them as 'fan charts' for the x=0.2, 0.6, 0.8 compositions in Figure 3. We subsequently analyze the magnetic field dependence of both hydrogenic and free carrier transitions to extract the exciton binding energy and reduced mass[36,37] of the exciton for each sample. High-energy absorption, observed only at high magnetic field (>30 T), is related to the free carrier transition between Landau levels in the valence and the conduction bands. The energy of this transition is given by:

$$E(B) = E_g + (n + \tfrac{1}{2})\hbar\omega_c \qquad (1)$$

where E_g is the band gap, n = 0, 1, 2, . . . represents the Landau orbital quantum number in the conduction and valence bands, $\omega_c = eB/\mu$ is the cyclotron frequency and $\mu^{-1}=m_e^{-1} + m_h^{-1}$ is the exciton reduced mass (m_e,m_h are the effective masses for electrons and holes, respectively). For dipole-allowed optical transitions ($\Delta n = 0$), the only fitting parameter is the exciton reduced mass μ, which provides a strong constraint to its value. The results of the fit are given by blue solid line in Fig. 3.

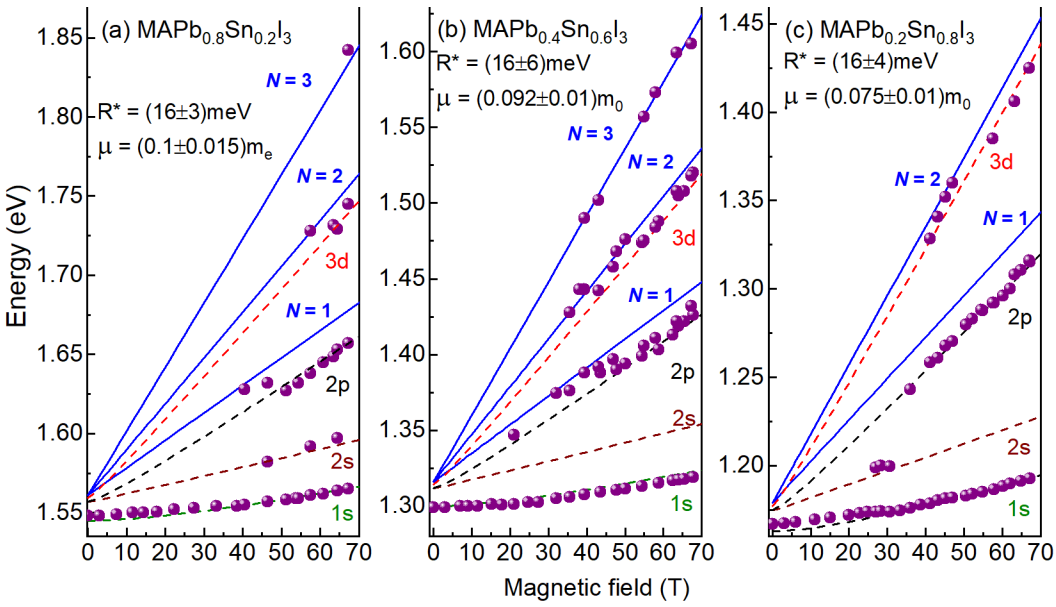

Figure 3: Energy Landau fan chart. Excitonic transition and inter Landau level transition energies as a function of magnetic field at 2 K for (a) $MAPb_{0.8}Sn_{0.2}I_3$, (b) $MAPb_{0.4}Sn_{0.6}I_3$ and (c) $MAPb_{0.2}Sn_{0.8}I_3$ thin films. Dashed lines

represent the results of the fit of hydrogen-like transitions. Blue lines indicate fitting results of the interband transition between Landau levels.

Next, we consider low energy transitions related to the excitonic states, which is described with a hydrogen-like model in a magnetic field[48]. This numerical model describes the magnetic field dependence of energies of free exciton states $E_{n,0}(\gamma)$ with a dimensionless parameter $\gamma=\hbar\omega_c/2R^*$. Here, the effective Rydberg constant $R^* = R_0\mu/m_0\varepsilon_{eff}^2$ represents the exciton binding energy, where R_0 denotes the atomic Rydberg constant, m_0 is the free electron mass and ε_{eff} is the relative dielectric constant. We fit $E_{n,0}(\gamma)$ (dashed lines in Fig. 3) using $\hbar\omega_c$ calculated from values of μ obtained in the previous step, hence R* remains as the only fitting parameter. However, similarly to our previous studies[37,38], we find that the strongest constraint on the value of R* is provided by simultaneous observation of the 1s and higher excitonic transitions (particularly the 2s state, only observable once their oscillator strength has been enhanced by the magnetic field). This condition allows a precise determination of eigenenergies of an excitonic system in zero magnetic field given by:

$$E_n = E_g - \frac{R^*}{n^2} \qquad (2)$$

where E_n is the energy of n_{th} excitonic level. Thus, it is worth emphasizing that in our studies R* and μ are determined directly, without any assumption on the value of effective dielectric constant. We note that collecting a sufficient number of data points to construct conclusive fan charts turns out to be more challenging in the case of Pb:Sn alloys than in the pure-Pb counterparts we investigated earlier[36–38]. This originates from both intrinsic inhomogeneity and instability of Pb:Sn films, resulting in broadened and less resolved absorption minima. Therefore, we limit our report to three best characterized compositions, among which are low (x = 0.2), intermediate (x = 0.6) and high (x = 0.8) tin content, which allow us to draw conclusions.

The values of μ and R^* obtained for the three Pb:Sn compositions are summarized in Table 1 and plotted as a function of the bandgap in Figure 4, together with our previous results for the wider bandgap lead halide

perovskites[36–38]. The exciton reduced mass μ (Fig. 4(a)) decreases as we increase the tin content, from (0.095 ± 0.010) m_0 for x = 0.2 to (0.075 ± 0.010) m_0 for x = 0.8, where m_0 indicates the free electron mass. These results are in a good agreement with density functional theory (DFT) calculations for $MAPb_{1-x}Sn_xI_3$ compounds, which yield values of μ ranging from 0.07 m_0 to 0.10 m_0[41,49]. We observe that the reduced mass follows the band gap, extending the trend we previously found for the larger bandgap lead halide perovskites. We therefore can generalize the reduced mass versus bandgap dependence across a broad range of perovskite absorbers (~1.2 – 2.4 eV bandgap) using the empirical two-band k.p approach[37,50]. Assuming the approximation $m_e = m_h$, the reduced mass of the exciton can be written as:

$$\frac{1}{\mu} = \frac{4|P|^2}{m_0 E_g} \quad (3)$$

where $P = \langle \Psi_{VB}|p_x|\Psi_{CB}\rangle$ is the momentum matrix element which couples the electronic states in the conduction and valence bands. Finally, $2|P|^2/m_0$ is the Kane energy, a parameter defining the coupling of valence and conduction bands, which we find to be (8.7 ± 0.3) eV after fitting Eq.3 to the experimental data covering the whole 1.2 – 2.4 eV bandgap range. Such result only slightly exceeds the theoretical predictions, suggesting the range from 5 to 7 eV[41,51]. As the effective mass of carriers is one of the parameters that determines charge transport properties in semiconductors, understanding how this quantity changes with varying chemical composition (i.e. bandgap) is essential for identifying the impact of alloying Pb:Sn on properties that govern optoelectronic device operation. The strong dependence on bandgap also suggests that we can controllably tune the effective mass through judicial changes in composition.

Table 1: The parameters of the fit of the energy fan chart for $MAPb_{1-x}Sn_xI_3$ perovskites at T = 2 K

Compound	E_g (meV)	R_* (meV)	μ (m_0)	ε_{eff}
$MAPb_{0.8}Sn_{0.2}I_3$	1560	16 ± 3	0.100 ± 0.01	9.2 ± 1.5
$MAPb_{0.4}Sn_{0.6}I_3$	1310	16 ± 6	0.092 ± 0.01	8.9 ± 2.1

$MAPb_{0.2}Sn_{0.8}I_3$	1195	16 ± 4	0.075 ± 0.01	8.0 ± 1.6

We show our experimental estimations for exciton binding energies R* in Fig. 4(b). We find R* is around 16 meV for all investigated compositions, which is comparable to values of R* in $APbI_3$ perovskites we reported previously[37,38]. However, in this study of Pb:Sn alloys we assume that experimental errors for R* are larger by around a factor of three due to limited data points for higher excitonic transitions. While this uncertainty restricts us from concluding firmly that the expected R* (E_G) linear trend is conserved, we still can provide firm upper bounds for the exciton binding energy; in the end the upper bound is the most important quantity for describing device operation. These low temperature values of R*, already smaller than the mean thermal energy at room temperature (≈ 26 meV), are expected to drop further at higher temperatures when the dynamic disorder in the lattice enhances the dielectric screening[42]. We have experimentally demonstrated for hybrid lead iodides that at room temperature the value of R* is reduced by at least 20% with respect to the low-temperature orthorhombic phase[36,37,52]. This strongly suggests that at the temperatures corresponding to the typical operational conditions of solar cells, the dominant photo-generated species in Pb:Sn mixed perovskites is free carriers, and such an ease of carrier separation clearly contributes to the excellent photovoltaic performance of these materials in planar heterojunction solar cells.

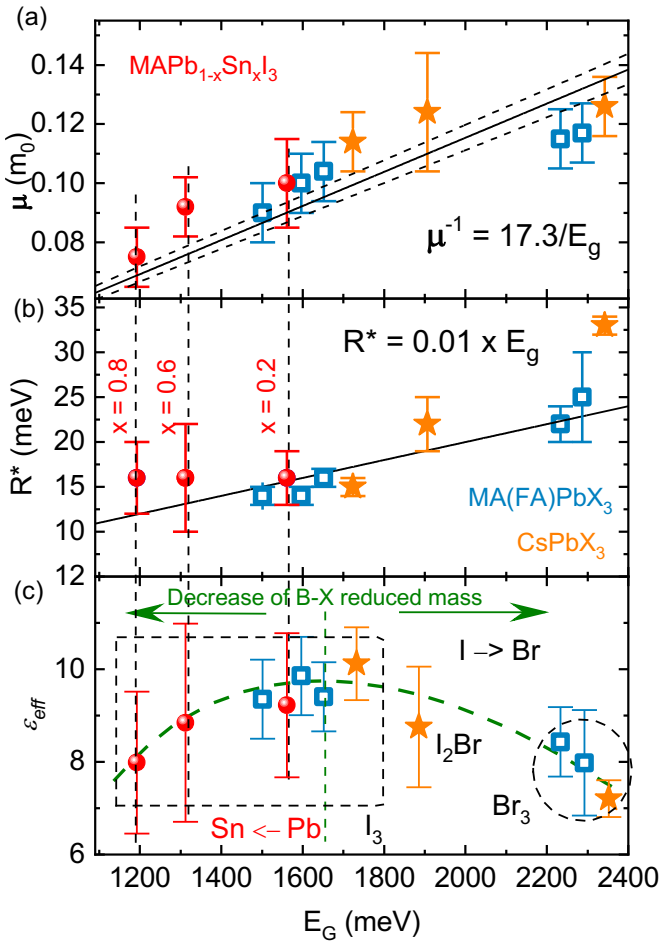

Figure 4: (a) Reduced mass, (b) binding energy and (c) dielectric constant as a function of the bandgap. The results for $MAPb_{1-x}Sn_xI_3$ family (red dots) compared with results from our previous work on organo-lead halides[36,37] (blue symbols) and fully inorganic $CsPbX_3$ compounds[38] (orange stars). Dashed parabola in panel (c) is a guide for an eye, suggesting the evolution of the reduced mass for B-X optical phonon mode.

Finally, having both R^* and μ extracted independently, we back-calculate ε_{eff}, which we plot as function of the bandgap in Fig. 4(c). Our earlier studies of Pb-based perovskites have shown that at low temperatures, when the movement of A-site cations is effectively frozen, the dielectric constant is determined by the halide composition of the PbX_6 octahedra[38]. In particular, we demonstrated that the εeff decreases as I is substituted with lighter Br. Such a behavior has been predicted

by theoretical calculations of the dielectric function in relation to the frequency of Pb-X stretching and Pb-X-Pb rocking modes, increasing for lighter halides[53,54]. The energy of optical phonon modes is inversely proportional to the reduced mass of the contributing atoms, therefore, one can expect that a substitution of either B or X site ion with a lighter counterpart reduces the value of ε_{eff}. While the experimental errors cannot be disregarded, our results for $MAPb_{1-x}SnxI_3$ family also suggest such a scenario, with the ε_{eff} obtained for $MAPb_{0.2}Sn_{0.8}I_3$ falling around 20% below the maximum corresponding to "heavy" PbI_6 octahedra. This motivates further studies, e.g. Raman spectroscopy[55], to investigate if the hardening of the phonon modes upon increasing Sn content prevents the values of R* from following the bandgap decrease.

In conclusion, we have studied the fundamental properties of the low bandgap $MAPb_{1-x}Sn_xI_3$ (x=0–1) perovskite family, revealing the temperature-dependent bandgap and phase transition behavior, as well as directly deriving key parameters including the exciton binding energy and effective mass. We find that increasing the content of Sn reduces the temperature of the phase transition from tetragonal to orthorhombic structure, from 162 K (x=0) to 105 K (x=1). We also reveal that an upper bound to the exciton binding energy is as low as 16 meV at low temperature for all compositions, which is similar to the values found in pure lead-based triiodide perovskites. However, the effective mass decreases from (0.095 ± 0.010)m_e (x=0.2) to (0.075 ± 0.010)m_e (x=0.8) with increasing Sn content, which follows the bandgap dependence seen previously for other lead halide perovskites. We therefore extend this model now to cover the wide bandgap range 1.2 – 2.4 eV. We conclude that although adding increasing fractions of Sn substantially changes the bandgap behavior, we do not significantly change the key fundamental properties

relevant to solar cell operation from those in their lead-only counterparts. In fact, the empirical bandgap dependence allows us to estimate these parameters from the bandgap alone, providing device design guidelines for new 3D perovskite materials with different bandgaps that will inevitably be generated. Therefore, we expect that there is no fundamental limitation to the mixed Pb/Sn perovskites from performing as well or even better than their lead-only analogues in optoelectronic devices.

Experimental Methods

Perovskite precursor solutions were synthesized by dissolving lead iodide (PbI2) or tin iodide (SnI2) and methylammonium chloride (MACl) in a 1:1 molar stoichiometric ratio in N,N-dimethylformamide (DMF) to obtain 0.15 M solutions. The mixture perovskite precursors were prepared by mixing the corresponding ratio of pure lead and tin perovskite precursor solutions.
Fused silica substrates were cleaned using ultrasonication in acetone and isopropanol for 15 min, respectively, after which the cleaned substrates were treated under oxygen plasma for 10 min. The perovskite thin-films were prepared in nitrogen filled glovebox adopting elevated temperature processing method[24]. Precursor solutions and substrates were heated at 80 ˚C and 240 ˚C, respectively, and then precursor solutions were spin-coated on substrates taken from hotplate at 4000 for 10 s followed by annealing for 10 min at 100 ˚C.

All optical measurements have been performed in LNCMI Toulouse. Magneto transmission spectra have been acquired using the long pulse magnetic field technique for magnetic fields up to 68 T and typical pulse duration of 100 ms. For the measurements, the sample was placed in a liquid helium/ exchange gas variable temperature insert, providing the temperature range from below 2 K up to 300 K. A halogen lamp was used as the white light source. The light emitted from the lamp was coupled in a 200 μm diameter multimode fiber, used to illuminate the sample. The transmitted light was coupled in a 400 μm diameter multimode fiber and guided to a spectrometer equipped with a liquid nitrogen cooled, fast read-out CCD camera. The exposure time reduced to 2ms ensured

that the transmission spectra were acquired at an essentially constant magnetic field value. Due to their limited stability in air at room temperature, the samples were manipulated in atmospheric conditions for less than 4 minutes, reducing the decomposition rate to the minimum.

Supporting information. Temperature-dependent transmission spectra for $MAPb_{0.2}Sn_{0.8}I_3$, $MAPb_{0.4}Sn_{0.6}I_3$ and $MAPbSnI_3$. 1s transition energies as a function of temperature for all investigated $MAPb_{1-x}Sn_xI_3$ compounds. Magneto-transmission spectra for $MAPb_{0.2}Sn_{0.8}I_3$, and $MAPb_{0.4}Sn_{0.6}I_3$.

Corresponding Authors

*E-mail: paulina.plochocka@lncmi.cnrs.fr (P.P)

*E-mail: sds65@cam.ac.uk (S.D.S)

Notes

The authors declare no competing financial interest.

Acknowledgements

This work was partially supported by BLAPHENE and STRABOT projects, which received funding from the IDEX Toulouse, Emergence program, "Programme des Investissements d'Avenir'" under the program ANR-11-IDEX-0002-02, reference ANR-10-LABX-0037-NEXT. M.B.and K.G. appreciate support from the Polish Ministry of Science and Higher Education within the Mobilnosc Plus program (grant no.\ 1648/MOB/V/2017/0 and 1603/MOB/V/2017/0). This work was supported by EPSRC (U.K.) via its membership to the EMFL (Grant No. EP/N01085X/1). S.D.S acknowledges the Royal Society and Tata Group (UF150033). The work was supported by a Royal Society International Exchanges Cost Share award (IECnR2n170108).

References

(1) Tan, Z.-K.; Moghaddam, R. S.; Lai, M. L.; Docampo, P.; Higler, R.; Deschler, F.; Price, M.; Sadhanala, A.; Pazos, L. M.; Credgington, D.; et al. Bright Light-Emitting Diodes Based on Organometal Halide Perovskite. *Nat. Nanotechnol.* **2014**, *9* (9), 687–

692.

(2) Adjokatse, S.; Fang, H.-H.; Loi, M. A. Broadly Tunable Metal Halide Perovskites for Solid-State Light-Emission Applications. *Mater. Today* **2017**, *20* (8), 413–424.

(3) Zhu, H.; Fu, Y.; Meng, F.; Wu, X.; Gong, Z.; Ding, Q.; Gustafsson, M. V; Trinh, M. T.; Jin, S.; Zhu, X. Y. Lead Halide Perovskite Nanowire Lasers with Low Lasing Thresholds and High Quality Factors. *Nat. Mater.* **2015**, *14* (6), 636–642.

(4) He, X.; Liu, P.; Wu, S.; Liao, Q.; Yao, J.; Fu, H. Multi-Color Perovskite Nanowire Lasers through Kinetically Controlled Solution Growth Followed by Gas-Phase Halide Exchange. *J. Mater. Chem. C* **2017**, *5* (48), 12707–12713.

(5) Fang, Y.; Dong, Q.; Shao, Y.; Yuan, Y.; Huang, J. Highly Narrowband Perovskite Single-Crystal Photodetectors Enabled by Surface-Charge Recombination. *Nat. Photonics* **2015**, 679–686.

(6) Wang, H.; Kim, D. H. Perovskite-Based Photodetectors: Materials and Devices. *Chem. Soc. Rev.* **2017**, *46* (17), 5204–5236.

(7) Tanaka, K.; Takahashi, T.; Ban, T.; Kondo, T.; Uchida, K.; Miura, N. Comparative Study on the Excitons in Lead-Halide-Based Perovskite-Type Crystals $CH_3NH_3PbBr_3$ $CH_3NH_3PbI_3$. *Solid State Commun.* **2003**, *127* (9), 619–623.

(8) Eperon, G. E.; Stranks, S. D.; Menelaou, C.; Johnston, M. B.; Herz, L. M.; Snaith, H. J. Formamidinium Lead Trihalide: A Broadly Tunable Perovskite for Efficient Planar Heterojunction Solar Cells. *Energy Environ. Sci.* **2014**, *7* (3), 982.

(9) Stranks, S. D.; Snaith, H. J. Metal-Halide Perovskites for Photovoltaic and Light-Emitting Devices. *Nat. Nanotechnol.* **2015**, *10* (5), 391–402.

(10) Stranks, S. D.; Eperon, G. E.; Grancini, G.; Menelaou, C.; Alcocer, M. J. P.; Leijtens, T.; Herz, L. M.; Petrozza, A.; Snaith, H. J. Electron-Hole Diffusion Lengths Exceeding 1 Micrometer in an Organometal Trihalide Perovskite Absorber. *Science (80-.).* **2013**, *342* (6156), 341–344.

(11) Xing, G.; Mathews, N.; Sun, S.; Lim, S. S.; Lam, Y. M.; Grätzel, M.; Mhaisalkar, S.; Sum, T. C. Long-Range Balanced Electron-and Hole-Transport Lengths in Organic-Inorganic $CH_3NH_3PbI_3$. *Science (80-.).* **2013**, *342* (6156), 344–347.

(12) Burschka, J.; Pellet, N.; Moon, S.-J.; Humphry-Baker, R.; Gao, P.; Nazeeruddin, M. K.; Grätzel, M. Sequential Deposition as a Route to High-Performance Perovskite-Sensitized Solar Cells. *Nature* **2013**, *499* (7458), 316–319.

(13) Liu, M.; Johnston, M. B.; Snaith, H. J. Efficient Planar Heterojunction Perovskite Solar Cells by Vapour Deposition. *Nature* **2013**, *501* (7467), 395–398.

(14) Shockley, W.; Queisser, H. J. Detailed Balance Limit of Efficiency of P-n Junction Solar Cells. *J. Appl. Phys.* **1961**, *32* (3), 510–519.

(15) Leijtens, T.; Bush, K. A.; Prasanna, R.; McGehee, M. D. Opportunities and Challenges for Tandem Solar Cells Using Metal Halide Perovskite Semiconductors. *Nat. Energy* **2018**, *3*, 828–838.

(16) Hörantner, M. T.; Leijtens, T.; Ziffer, M. E.; Eperon, G. E.; Christoforo, M. G.; McGehee, M. D.; Snaith, H. J. The Potential of Multijunction Perovskite Solar Cells. *ACS Energy Lett.* **2017**, *2* (10), 2506–2513.

(17) Noel, N. K.; Stranks, S. D.; Abate, A.; Wehrenfennig, C.; Guarnera, S.; Haghighirad, A.-A.; Sadhanala, A.; Eperon, G. E.; Pathak, S. K.; Johnston, M. B.; et al. Lead-Free Organic-Inorganic Tin Halide Perovskites for Photovoltaic Applications. *Energy Environ. Sci.* **2014**, *7* (9), 3061–3068.

(18) Hao, F.; Stoumpos, C. C.; Cao, D. H.; Chang, R. P. H.; Kanatzidis, M. G. Lead-Free Solid-State Organic - Inorganic Halide Perovskite Solar Cells. *Nat. Photonics* **2014**, *8* (6), 489–494.

(19) Shao, S.; Liu, J.; Portale, G.; Fang, H.-H.; Blake, G. R.; ten Brink, G. H.; Koster, L. J. A.; Loi, M. A. Highly Reproducible Sn-Based Hybrid Perovskite Solar Cells with 9% Efficiency. *Adv. Energy Mater.* **2017**, *8* (4), 1702019.

(20) Saliba, M.; Matsui, T.; Seo, J.-Y.; Domanski, K.; Correa-Baena, J.-P.; Nazeeruddin, M. K.; Zakeeruddin, S. M.; Tress, W.; Abate, A.; Hagfeldt, A. Cesium-Containing Triple Cation Perovskite Solar Cells: Improved Stability, Reproducibility and High Efficiency. *Energy Environ. Sci.* **2016**, *9* (6), 1989–1997.

(21) Saliba, M.; Matsui, T.; Domanski, K.; Seo, J.-Y.; Ummadisingu, A.; Zakeeruddin, S. M.; Correa-Baena, J.-P.; Tress, W. R.; Abate, A.; Hagfeldt, A. Incorporation of Rubidium Cations into Perovskite Solar Cells Improves Photovoltaic Performance. *Science (80-.).* **2016**, *354* (6309), 206–209.

(22) Hao, F.; Stoumpos, C. C.; Chang, R. P. H.; Kanatzidis, M. G. Anomalous Band Gap Behavior in Mixed Sn and Pb Perovskites Enables Broadening of Absorption Spectrum in Solar Cells. *J. Am. Chem. Soc.* **2014**, *136* (22), 8094–8099.

(23) Im, J.; Stoumpos, C. C.; Jin, H.; Freeman, A. J.; Kanatzidis, M. G. Antagonism between Spin-Orbit Coupling and Steric Effects Causes Anomalous Band Gap Evolution in the Perovskite Photovoltaic Materials $CH_3NH_3Sn_{1-x}Pb_xI_3$. *J. Phys. Chem. Lett.* **2015**, *6* (17), 3503–3509.

(24) Zhao, B.; Abdi-Jalebi, M.; Tabachnyk, M.; Glass, H.; Kamboj, V. S.; Nie, W.; Pearson,

A. J.; Puttisong, Y.; Gödel, K. C.; Beere, H. E.; et al. High Open-Circuit Voltages in Tin-Rich Low-Bandgap Perovskite-Based Planar Heterojunction Photovoltaics. *Adv. Mater.* **2016**, *29* (2), 1604744.

(25) Eperon, G. E.; Leijtens, T.; Bush, K. A.; Prasanna, R.; Green, T.; Wang, J. T.-W.; McMeekin, D. P.; Volonakis, G.; Milot, R. L.; May, R.; et al. Perovskite-Perovskite Tandem Photovoltaics with Optimized Band Gaps. *Science (80-.).* **2016**, *354* (6314), 861–865.

(26) Kanhere, P.; Chakraborty, S.; Rupp, C. J.; Ahuja, R.; Chen, Z. Substitution Induced Band Structure Shape Tuning in Hybrid Perovskites $CH_3NH_3Pb_{1-x}Sn_xI_3$ for Efficient Solar Cell Applications. *RSC Adv.* **2015**, *5* (130), 107497–107502.

(27) Pisanu, A.; Mahata, A.; Mosconi, E.; Patrini, M.; Quadrelli, P.; Milanese, C.; Angelis, F. De; Malavasi, L. Exploring the Limits of Three-Dimensional Perovskites: The Case of $FAPb_{1-x}Sn_xBr_3$. *ACS Energy Lett.* **2018**, 1353–1359.

(28) Goyal, A.; McKechnie, S.; Pashov, D.; Tumas, W.; van Schilfgaarde, M.; Stevanović, V. Origin of Pronounced Nonlinear Band Gap Behavior in Lead-Tin Hybrid Perovskite Alloys. *Chem. Mater.* **2018**, *30* (11), 3920–3928.

(29) Bis, R. F.; Dixon, J. R. Applicability of Vegard's Law to the $Pb_xSn_{1-x}Te$ Alloy System. *J. Appl. Phys.* **1969**, *40* (4), 1918–1921.

(30) Vurgaftman, I.; Meyer, J. R.; Ram-Mohan, L. R. Band Parameters for III-V Compound Semiconductors and Their Alloys. *J. Appl. Phys.* **2001**, *89* (11), 5815–5875.

(31) Leijtens, T.; Prasanna, R.; Gold-Parker, A.; Toney, M. F.; McGehee, M. D. Mechanism of Tin Oxidation and Stabilization by Lead Substitution in Tin Halide Perovskites. *ACS Energy Lett.* **2017**, *2* (9), 2159–2165.

(32) Leijtens, T.; Prasanna, R.; Bush, K. A.; Eperon, G.; Raiford, J. A.; Gold-Parker, A.; Wolf, E. J.; Swifter, S. A.; Boyd, C. C.; Wang, H.-P.; et al. Tin-Lead Halide Perovskites with Improved Thermal and Air Stability for Efficient All-Perovskite Tandem Solar Cells. *Sustain. Energy Fuels* **2018**, *2*, 2450–2459.

(33) Kapil, G.; Ripolles, T. S.; Hamada, K.; Ogomi, Y.; Bessho, T.; Kinoshita, T.; Chantana, J.; Yoshino, K.; Shen, Q.; Toyoda, T.; et al. Highly Efficient 17.6% Tin-Lead Mixed Perovskite Solar Cells Realized through Spike Structure. *Nano Lett.* **2018**, *18* (2), 3600–3607.

(34) Lai, M. L.; Tay, T. Y. S.; Sadhanala, A.; Dutton, S. E.; Li, G.; Friend, R. H.; Tan, Z.-K. Tunable Near-Infrared Luminescence in Tin Halide Perovskite Devices. *J. Phys. Chem. Lett.* **2016**, *7* (14), 2653–2658.

(35) Lanzetta, L.; Marin-Beloqui, J. M.; Sanchez-Molina, I.; Ding, D.; Haque, S. A. Two-Dimensional Organic Tin Halide Perovskites with Tunable Visible Emission and Their Use in Light-Emitting Devices. *ACS Energy Lett.* **2017**, *2* (7), 1662–1668.

(36) Miyata, A.; Mitioglu, A.; Paulina, P.; Portugall, O.; Tse-Wei Wang, J.; Stranks, S. D.; Snaith, H. J.; Nicholas, R. J. Direct Measurement of the Exciton Binding Energy and Effective Masses for Charge Carriers in an Organic-Inorganic Tri-Halide Perovskite. *Nat. Phys.* **2015**, *11*, 582-U94.

(37) Galkowski, K.; Mitioglu, A.; Miyata, A.; Plochocka, P.; Portugall, O.; Eperon, G. E.; Wang, J. T.-W.; Stergiopoulos, T.; Stranks, S. D.; Snaith, H. J.; et al. Determination of the Exciton Binding Energy and Effective Masses for Methylammonium and Formamidinium Lead Tri-Halide Perovskite Semiconductors. *Energy Environ. Sci.* **2016**, *9* (3), 962–970.

(38) Yang, Z.; Surrente, A.; Galkowski, K.; Miyata, A.; Portugall, O.; Sutton, R. J.; Haghighirad, A. A.; Snaith, H. J.; Maude, D. K.; Plochocka, P.; et al. Impact of the Halide Cage on the Electronic Properties of Fully Inorganic Cesium Lead Halide Perovskites. *ACS Energy Lett.* **2017**, *2* (7), 1621–1627.

(39) Oku, T. Crystal Structures of $CH_3NH_3PbI_3$ and Related Perovskite Compounds Used for Solar Cells. In *Solar Cells - New Approaches and Reviews*; InTech, 2015.

(40) Takahashi, Y. Y.; Obara, R.; Lin, Z.-Z.; Takahashi, Y. Y.; Naito, T.; Inabe, T.; Ishibashi, S.; Terakura, K. Charge-Transport in Tin-Iodide Perovskite $CH_3NH_3SnI_3$: Origin of High Conductivity. *Dalt. Trans.* **2011**, *40* (20), 5563.

(41) Umari, P.; Mosconi, E.; De Angelis, F. Relativistic GW Calculations on $CH_3NH_3PbI_3$ and $CH3NH_3SnI_3$ Solar Cells. *Sci. Rep.* **2014**, *4*, 4467.

(42) Even, J.; Pedesseau, L.; Katan, C. Analysis of Multivalley and Multibandgap Absorption and Enhancement of Free Carriers Related to Exciton Screening in Hybrid Perovskites. *J. Phys. Chem. C* **2014**, *118* (22), 11566–11572.

(43) Huang, L.; Lambrecht, W. R. L. Electronic Band Structure, Phonons, and Exciton Binding Energies of Halide Perovskites $CsSnCl_3$, $CsSnBr_3$, and $CsSnI_3$. *Phys. Rev. B* **2013**, *88* (16), 165203.

(44) Singh, S.; Li, C.; Panzer, F.; Narasimhan, K. L.; Graeser, A.; Gujar, T. P.; Köhler, A.; Thelakkat, M.; Huettner, S.; Kabra, D. Effect of Thermal and Structural Disorder on the Electronic Structure of Hybrid Perovskite Semiconductor $CH_3NH_3PbI_3$. *J. Phys. Chem. Lett.* **2016**, *7* (15), 3014–3021.

(45) Galkowski, K.; Mitioglu, A. A.; Surrente, A.; Yang, Z.; Maude, D. K.; Kossacki, P.;

Eperon, G. E.; Wang, J. T.-W.; Snaith, H. J.; Plochocka, P.; et al. Spatially Resolved Studies of the Phases and Morphology of Methylammonium and Formamidinium Lead Tri-Halide Perovskites. *Nanoscale* **2017**, *9* (9), 3222–3230.

(46) Parrott, E. S.; Milot, R. L.; Stergiopoulos, T.; Snaith, H. J.; Johnston, M. B.; Herz, L. M. Effect of Structural Phase Transition on Charge-Carrier Lifetimes and Defects in $CH_3NH_3SnI_3$ Perovskite. *J. Phys. Chem. Lett.* **2016**, *7* (7), 1321–1326.

(47) Knutson, J. L.; Martin, J. D.; Mitzi, D. B. Tuning the Band Gap in Hybrid Tin Iodide Perovskite Semiconductors Using Structural Templating. *Inorg. Chem.* **2005**, *44* (13), 4699–4705.

(48) Makado, P. C.; McGill, N. C. Energy Levels of a Neutral Hydrogen-like System in a Constant Magnetic Field of Arbitrary Strength. *J. Phys. C Solid State Phys.* **1986**, *19* (6), 873.

(49) Umari, P.; Mosconi, E.; Angelis, F. De. Infrared Dielectric Screening Determines the Low Exciton Binding Energy of Metal-Halide Perovskites. *J. Phys. Chem. Lett.* **2018**, *9* (3), 620–627.

(50) Even, J.; Pedesseau, L.; Katan, C.; Kepenekian, M. M.; Lauret, J.-S.; Sapori, D.; Deleporte, E. Solid-State Physics Perspective on Hybrid Perovskite Semiconductors. *J. Phys. Chem. C* **2015**, *119* (19), 10161–10177.

(51) Menéndez-Proupin, E.; Palacios, P.; Wahnón, P.; Conesa, J. C. Self-Consistent Relativistic Band Structure of the $CH_3NH_3PbI_3$Perovskite. *Phys. Rev. B* **2014**, *90* (4), 045207.

(52) Yang, Z.; Surrente, A.; Galkowski, K.; Bruyant, N.; Maude, D. K.; Haghighirad, A. A.; Snaith, H. J.; Plochocka, P.; Nicholas, R. J. Unraveling the Exciton Binding Energy and the Dielectric Constant in Single-Crystal Methylammonium Lead Triiodide Perovskite. *J. Phys. Chem. Lett.* **2017**, *8* (8), 1851–1855.

(53) Berdiyorov, G. R.; Kachmar, A.; El-Mellouhi, F.; Carignano, M. A.; El-Amine Madjet, M. Role of Cations on the Electronic Transport and Optical Properties of Lead-Iodide Perovskites. *J. Phys. Chem. C* **2016**, *120* (30), 16259–16270.

(54) Feng, J.; Xiao, B. Effective Masses and Electronic and Optical Properties of Nontoxic $MASnX_3$ (X= Cl, Br, and I) Perovskite Structures as Solar Cell Absorber: A Theoretical Study Using HSE06. *J. Phys. Chem. C* **2014**, *118* (34), 19655–19660.

(55) Pérez-Osorio, M. A.; Milot, R. L.; Filip, M. R.; Patel, J. B.; Herz, L. M.; Johnston, M. B.; Giustino, F. Vibrational Properties of the Organic--Inorganic Halide Perovskite $CH_3NH_3PbI_3$ from Theory and Experiment: Factor Group Analysis, First-Principles

Calculations, and Low-Temperature Infrared Spectra. *J. Phys. Chem. C* **2015**, *119* (46), 25703–25718.